Hypersonic Flows in Large-Scale Inlet Models

William R. Seebaugh*
Fairchild Industries Inc., Farmingdale, N. Y.

Analytical and experimental investigations were conducted to determine the characteristics of the internal flows in model passages representative of inlets for a typical Mach 12 hypersonic cruise vehicle and also sufficiently large for reliable data to be obtained. Three large-scale inlet models, each having a different internal compression ratio, were designed to provide maximum performance at the throat stations. Tests were conducted in the Mach 7.4 nozzle of the NASA Ames 3.5-Foot Hypersonic Wind Tunnel at a nominal test Reynolds number of 2.7×10^6 per ft. The experimental results revealed that a high level of total pressure recovery, approximately 0.85 (relative to the inlet-entrance conditions) for the core flow of the internal passage, was achieved for each inlet design. Within the accuracy of the measurements, the recovery was in agreement with the predicted level and was independent of the internal compression ratio over the range tested.

Nomenclature

M = Mach number
P = pressure (psia)
T = temperature (°R)
U = streamwise velocity component (fps)
X,Y,Z = spatial coordinates (in.)
δ = boundary-layer thickness (in.)
δ^* = displacement thickness (in.)

Subscripts

e = boundary-layer edge
p = pitot
t = stagnation condition
∞ = tunnel freestream

Superscript

$()'$ = coordinate measured relative to a geometric surface

Introduction

THE aerodynamic performance of the air-induction system is an important factor in establishing the viability of a hypersonic vehicle design. The inlet performance is primarily a function of the internal contour design. The development and assessment of analytical techniques for the design of inlet contours are based on wind-tunnel tests of scale models of representative hypersonic inlets. Previous experimental investigations[1] have been performed with scale models of entire vehicle configurations. This procedure results in very small internal flow passages, and measurements of the internal flow properties are very difficult to obtain. Consequently, improvements in the methods used for designing and analyzing hypersonic air-induction systems depend, in a large part, on the development of techniques for testing relatively large-scale inlet models.

During the present investigation, a method was devised for testing a large-scale inlet model of one of the engine modules for the hypersonic vehicle configuration shown in Fig. 1. This vehicle, designed for operation in the Mach 10–12 range, employs a conical compression surface that forms the forebody and delivers air to the engine modules located circumferentially about the fuselage. Since the diameter of the hypersonic vehicle fuselage is large relative to the engine module height, the flow at the inlet entrance and within the internal passages is basically two-dimensional. In the present investigation, a wedge forebody was used to simulate the flowfield at the entrance of one of the engine modules for the vehicle of Fig. 1, thus removing the actual vehicle forebody from consideration in the design of the wind tunnel model. The resulting model configuration is shown schematically in Fig. 2.

Received May 1, 1972; revision received October 5, 1972. Work supported by NASA Contracts NAS2-5052 and NAS2-5719, under technical cognizance of Aerodynamics Branch, Ames Research Center.

Index categories: Hypersonic Airbreathing Propulsion; Aircraft and Component Wind Tunnel Testing; Supersonic and Hypersonic Flow.

*Project Manager, Preliminary Design, Fairchild Republic Div.; presently Member of Technical Staff, Science Applications Inc., Arlington, Va. Member AIAA.

Hypersonic Cruise Vehicle Considerations

Several design characteristics of the cruise vehicle shown in Fig. 1 were considered in the conceptual design of the inlet models for the present study. The vehicle design itself is discussed in detail in Ref. 1. The inlet-entrance Mach number for a given engine module depends upon the flight Mach number, the vehicle angle of attack, and the circumferential location of the engine module. A representative inlet-entrance Mach number of 6.0 was selected for the present study. The aerodynamic heating conditions encountered by a full-scale cruise vehicle dictated the use of cooled compression surfaces and some degree of bluntness for the cowl leading edge. No boundary-layer bleed was utilized in the inlet design for the vehicle discussed in Ref. 1, and the boundary layers comprised a significant portion of the mass flow captured by the inlets. For maximum thrust effectiveness, the flow direction at the inlet throat and through the combustor was nearly parallel to the longitudinal axis of the vehicle.

A wide variation of inlet compression ratio is desired when different applications are considered. The definition of compression ratio used in this paper is the ratio of the static pressure at the inlet throat to the static pressure at the inlet entrance (throat pressure/capture pressure). Internal-passage compression ratios of 2, 8, and 12 were selected for the present study.

Model Design

General Model Configuration

The experimental programs of the present investigation were conducted in the Mach 7.4 nozzle of the NASA

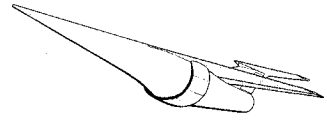

Fig. 1 Hypersonic cruise vehicle for Mach 10 to 12 range.

Ames 3.5-Foot Hypersonic Wind Tunnel. The facility is a blowdown tunnel with a run time of from 1 to 4 min at the nominal test conditions used in the investigation. Those conditions were: Mach number = 7.4, total pressure = 600 psia, total temperature = 1460 °R, and Reynolds number = 2.7×10^6 ft^{-1}.

The hypersonic vehicle design considerations and the characteristics of the wind tunnel were the primary factors in the selection of the basic model configuration. The representative inlet-entrance Mach number of 6.0 was simulated in the Mach 7.4 tunnel flow with a 7° wedge forebody. Simulation of the ratio of boundary-layer thickness to inlet height at the inlet entrance required that a turbulent boundary layer be established on the wedge forebody well upstream of the entrance to the internal passage. To provide sufficient length for boundary-layer development, while maximizing the inlet size, the wedge-forebody length (to the inlet-entrance station) and the height of the cowl lip above the forebody surface (Fig. 2) were the maximum allowable consistent with wind-tunnel blockage limitations, giving an internal passage size of approximately one-third of full scale. Complete simulation of the vehicle inlet-entrance conditions could not be achieved in the wind tunnel tests because the high flight enthalpy could not be reproduced experimentally.

Three internal passages, designated $P2$, $P8$, and $P12$ for internal compression ratios of 2, 8, and 12, respectively, were constructed. The wedge forebody, undercarriage, and sting support (Fig. 2) were common to all internal passages. The interchangeable internal passage sections could be rotated closed for protection of instrumentation during tunnel starting and to vary the contraction ratio to permit inlet starting. The wedge-forebody and compression surfaces were constructed of aluminum with stainless steel leading edges in exposed regions. The leading edges and the forward portions of the wedge-forebody and the cowl surfaces were water cooled. The combination of water cooling and the large masses of aluminum provided nearly isothermal wall conditions during the relatively short tunnel runs. The shielding of the internal passages from the tunnel flow during the tunnel starting process also aided in maintaining uniform and low surface temperatures within the internal passages.

Internal Contour Development

The minimum practical leading-edge diameter for a Mach 12 cruise vehicle using regenerative cooling is approximately 0.125 in. (Ref. 2). Since the model was approximately one-third scale, a leading-edge diameter of 0.045 in. was selected for the present investigation. The shock wave generated at the blunt-cowl leading edge immediately enters the internal passage and must be reduced in strength if the goal of maximum total pressure recovery at the inlet throat is to be realized. For a given leading-edge bluntness, the goal of maximum pressure recovery is achieved, in principle, if the cowl shock wave is cancelled at its first point of impingement upon the wedge forebody. The remaining flow to the throat is then shock-free. In the present investigation, the contours of the internal passages were designed to effect cancellation of the cowl shock wave at the centerbody surface. Early in the study it became evident that comparison of the experimentally measured performance of the three inlets (compression ratios of 2, 8, and 12) would be most meaningful if all inlets were designed for the same theoretical total-pressure recovery. This design requirement was satisfied by employing the same contour in the immediate region of the cowl leading edge and maintaining the same point of impingement of the cowl shock wave on the forebody surface for all internal passages.

The analytical techniques employed to design the internal contours and to predict the internal flow development

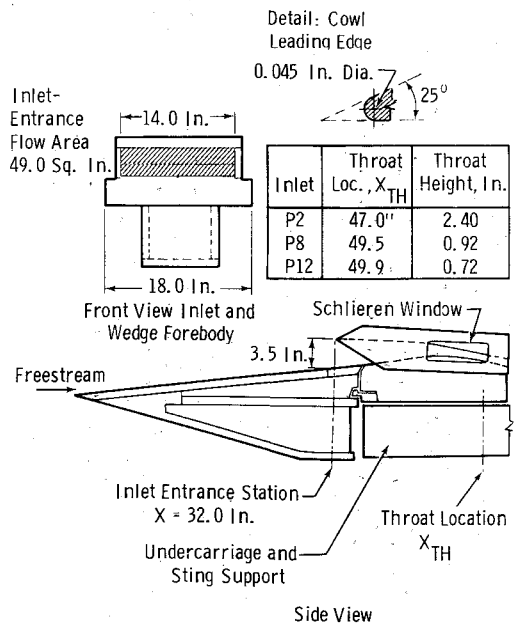

Inlet	Throat Loc., X_{TH}	Throat Height, In.
P2	47.0"	2.40
P8	49.5	0.92
P12	49.9	0.72

Fig. 2 Schematic representation of inlet model.

utilized a displacement-thickness correction scheme to account for the coupling between the boundary layers and the inviscid flowfields. Effective contours were first designed using the method of characteristics for two-dimensional flows. (The effective surface coordinate at any point is the sum of the geometric surface coordinate of the model itself and the boundary-layer displacement thickness.) The effective centerbody contour for each inlet was simply a 7° wedge upstream of the point of shock-wave cancellation. The shape of each effective cowl contour was primarily a function of the rate of compression on the cowl surface, which was highest for the $P12$ inlet model. The cowl surfaces for the lower compression inlets were essentially derivatives of the $P12$ design. The effective centerbody surface downstream of the point of shock-wave cancellation for each inlet was designed by cancelling the compression waves that were associated with the turning of the cowl surface. Utilizing a procedure analogous to that used in nozzle contour design, essentially parallel flow was obtained at the throat station for each inlet.

Predictions for the surface pressure distributions for the three inlets are shown in Fig. 3. The cowl shock wave impinges upon the centerbody surface of each inlet at X = 44.25 in. After the shock wave is cancelled by turning the centerbody surface, the centerbody static pressure for the $P12$ inlet increases monotonically to the design ratio of 37.5 (P/P_∞ = 37.5, where P/P_∞ = 3.135 at the inlet-entrance station) at X = 49.6 in. The compressive turning of

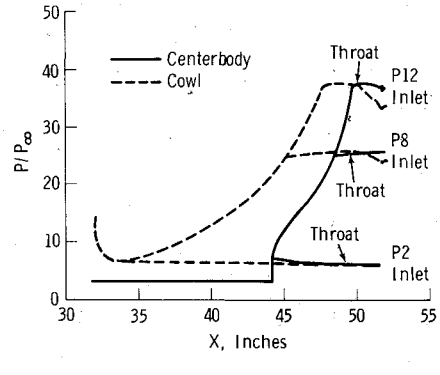

Fig. 3 Predicted surface static-pressure distributions.

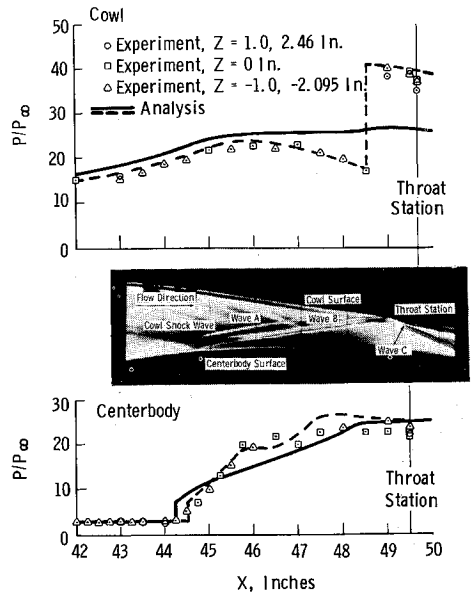

Fig. 4 Surface static-pressure distributions and flowfield pattern, P8 inlet model.

the cowl surface for the $P12$ inlet ends at X = 48.0 in., where the design ratio of 37.5 is attained.

Observation of the surface static-pressure distributions for the $P12$ inlet (Fig. 3) shows that the design pressure ratio for the $P8$ inlet ($P/P_\infty = 25.0$) is reached at $X = 48.5$ in. on the $P12$ inlet centerbody and at X = 45.3 in. on the $P12$ inlet cowl. The contours for the $P8$ inlet were derived from the $P12$ inlet contours by using the existing contours up to the aforementioned stations and eliminating any further turning.

The design pressure ratio for the $P2$ inlet ($P/P_\infty = 6.25$) is lower than the minimum surface static-pressure ratio achieved by the $P8$ and $P12$ inlets (Fig. 3); therefore the internal passage for the $P2$ inlet must provide an expanding flowfield. The contours of the $P2$ inlet were obtained by using the $P8$ and $P12$ inlet contours for the centerbody up to the point of shock-wave cancellation (X = 44.25 in.) and for the cowl up to X = 34.0 in., and then expanding the flow slightly to the throat, $X = 47.0$ in.

The pressure distributions presented in Fig. 3 and the corresponding velocity distributions were used as edge conditions to compute the boundary-layer development for the nominal wind-tunnel test conditions. The calculations for the wedge-forebody and centerbody were obtained (Ref. 3) using a modification of the method reported by Reshotko and Tucker. The method of Clutter and Smith (Ref. 4) was used to compute the boundary-layer development on each cowl surface, under the assumption that the boundary layer remained laminar over the entire cowl length.

The geometric model surfaces for the wedge-forebody and internal contours were obtained, in most regions, by subtracting the computed boundary-layer displacement thickness distributions from the effective contours designed by the method of characteristics. A special procedure was applied for the shock-wave cancellation regions to account for the boundary-layer development across the shock-induced pressure increases. Simple subtraction of the computed displacement thicknesses from the effective contours yields geometric contours with forward-facing steps. Since contours of this nature were unacceptable, the changes in boundary-layer displacement thickness across the cancellation regions were recomputed using a control volume approach similar to that of Ref. 5. The contours formed by subtracting these changes in displacement thickness from the effective contours over the interaction-region lengths given by the correlation of Pinckney[6] were faired into the previously developed geometric contour segments upstream and downstream of the interaction regions.

Instrumentation

The tunnel total pressure P_{t_∞} was sensed by a probe located within the settling chamber of the wind tunnel. The tunnel total temperature T_{t_∞} was measured in the freestream below the leading edge of the model. The tunnel Mach number M_∞ and static pressure P_∞ were computed from the wind-tunnel calibrations using the tunnel total pressure and a temperature measured in the heater section of the wind tunnel.

Surface pressures on the wedge forebody and within the internal passages of the inlet models were sensed by 0.0625-in. diam orifices and read using absolute strain-gage pressure transducers. Surface temperatures were measured using chromel-alumel thermocouple junctions imbedded in the surfaces.

Pitot pressure measurements were obtained using 0.040-in. diam stainless steel tubes with either round tips (for inviscid flow measurements) or tubes flattened to 0.020-in. height (for boundary-layer surveys). Static pressures were measured using an 0.020-in. diameter probe with four interconnected measuring orifices located on the probe shaft. Two designs for total temperature probes were employed: a singly shielded, aspirating probe with a chromel-alumel thermocouple junction located within the probe tube, and an exposed thermocouple probe with a chromel-alumel thermocouple junction oriented normal to the stream between two insulated support tubes.

Results and Discussion

Experimental results and analytical predictions for the surface pressure distributions and flowfield properties are given in this paper for the $P8$ inlet model, which is considered to be the most representative inlet model of those tested for application to the hypersonic cruise vehicle shown in Fig. 1. Complete results for the wedge-forebody flowfield and for the three inlet models are given in Refs. 7 and 8.

Inlet-Entrance Flowfield

The flowfield at the inlet-entrance station provides the basis for evaluation of the performance of the internal

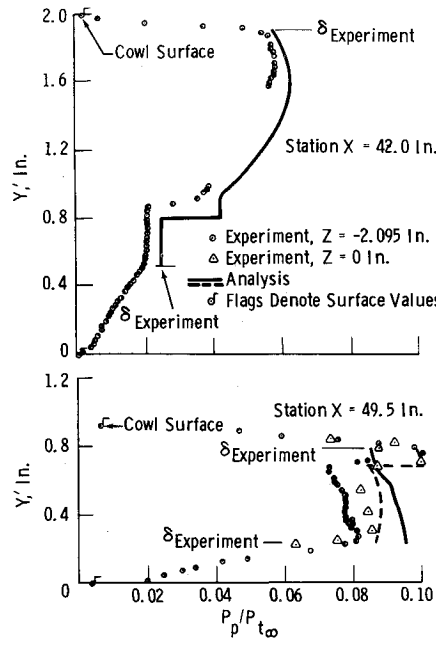

Fig. 5 Pitot-pressure distributions, P8 inlet model.

passages. The design flowfield at the inlet-entrance station was that produced by a 7° wedge in a uniform stream at a Mach number M_∞ of 7.4. The predicted flowfield properties for this condition were: Mach number M = 6.032, static pressure ratio P/P_∞ = 3.135, and total pressure recovery P_t/P_{t_∞} = 0.863. The experimental results obtained at the inlet-entrance station are presented and analyzed in Refs. 7 and 8. The experimentally determined total pressure recovery at the inlet-entrance station varied from 0.73 to 0.97, with an average value of 0.8. The variations about this level are a result of the extreme sensitivity of total pressure recovery to scatter in the experimental data in the Mach number range of interest.

The turbulent nature of the wedge-forebody boundary layer at the inlet-entrance station, which was an important factor in the proper simulation of the inlet-entrance flowfield, was verified by measuring the local surface shearing stress with a skin-friction gage and by observation of the boundary-layer profiles. Transition from laminar to turbulent boundary-layer flow occurred on the wedge forebody at about X = 14.0 in. This result was obtained using a fluorine-sublimation technique.

Internal Passage Flowfield

Surface Measurements and Probe Surveys

Surface static-pressure distributions and the internal flowfield pattern are shown in Fig. 4 for the *P*8 inlet model. The cowl shock wave enters the centerbody boundary layer at the upstream edge of the schlieren window and a complex reflected wave system emerges farther downstream. The reflected wave system interacts with the cowl boundary layer and again enters the inviscid flowfield near the throat station, X = 49.5 in. The results of experimental profile surveys, surface oil-flow studies, and observations of a number of black-and-white and color schlieren photographs reveal the following characteristics of the reflected wave system:

1) Weak shock waves propagate from the corners formed by the intersections of the swept sidewalls and the centerbody surface toward the centerline of the internal passage; 2) The cowl shock wave curves upstream in the regions between the corner shock waves and sidewalls, generating the first light band of the reflected wave system (Wave *A*, Fig. 4). This wave exists only near the sidewalls; 3) The

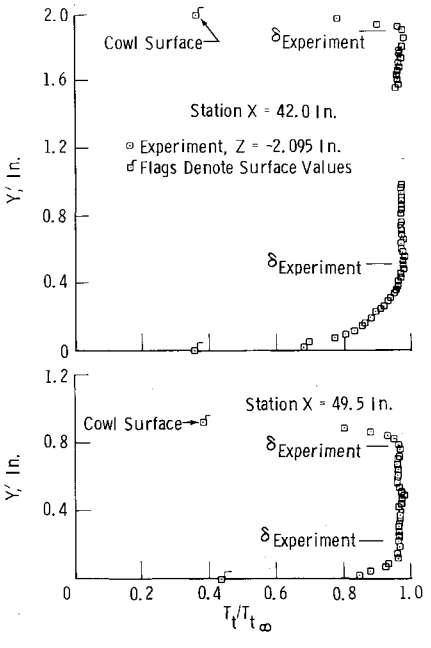

Fig. 6 Total-temperature distributions, P8 inlet model.

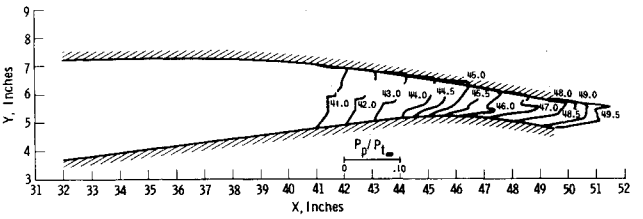

Fig. 7 Summary of experimental pitot-pressure distributions, P8 inlet model.

cowl shock wave is straight over the central portion of the passage, and the reflection from the centerbody occurs farthest downstream in this central region. The reflected shock wave is slightly curved (in the lateral direction) between the central region and the areas swept by the corner shock waves. This curvature causes the apparent multiple-wave appearance of the main reflected shock wave (Wave *B*); 4) The reflected shock wave impinges upon the cowl surface at approximately X = 48.8 in. and the wave reflected from the cowl surface propagates toward the center of the passage (Wave *C*); and 5) No evidence of boundary-layer separation was observed in the regions of high adverse pressure gradient.

The measured surface-static pressures on the centerbody are quite unlike the original predictions (solid lines in Fig. 4). A slight decrease in pressure occurs in the region of surface curvature between X = 43.4 in., which is the beginning of the faired portion of the shock-wave cancellation surface, and the steep pressure rise caused by the shock-wave reflection process. The centerbody static pressure surpasses the prediction at X = 45.25 in., undergoes a series of oscillations, and finally reaches a nearly constant value equal to about 90% of the design level between X = 47.5 and 49.5 in. The experimental cowl pressures fall below the original prediction upstream of approximately X = 48.5 in. The reflected shock wave impinges upon the cowl surface at about X = 48.8 in., and the experimental pressure level exceeds the prediction downstream of this station. Most of the discrepancies between the predicted and measured static pressure distributions were resolved by modifying the analysis to reflect pertinent experimental measurements not taken into account in the original design procedure (e.g., wind-tunnel flow nonuniformities, boundary-layer transition locations, etc.). The method of analysis of the centerbody shock-wave boundary-layer interaction was also modified to account for a strong expansion that is formed as the cowl shock wave enters the centerbody boundary layer near X = 43.0 in. and also to include the main reflected shock wave. The expansion, as noted by Rose in Ref. 9, is not overtaken by the reflected shock wave and both waves impinge upon the cowl surface. The results of the revised analysis, shown by the dashed lines in Fig. 4, are in good agreement with experiment. It may also be concluded that complete cancellation of the reflected shock wave by simply turning the centerbody surface may not be possible because of the influence of the aforementioned expansion wave; however, the strength of the reflected shock wave may be reduced by this approach.

Pitot pressures and total temperatures were measured at 13 stations within the *P*8 internal passage. Typical survey results, adjusted to the nominal tunnel conditions, are presented in Figs. 5 and 6. The pitot pressure profile at X = 42.0 in. shows the apparent edges of the boundary layers on both inlet surfaces and the location of the cowl shock wave. The pitot pressure increases rapidly as the probe moves above the shock wave and then continues to increase in the compression region between the shock wave and the edge of the cowl boundary layer. As shown in the schlieren photograph of Fig. 4, the shock wave has reflected from the cowl surface and again entered the central

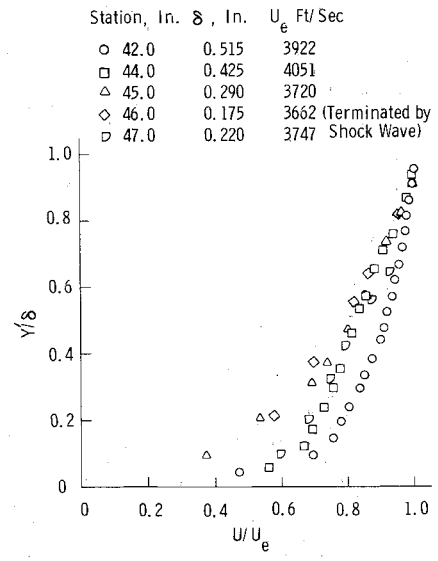

Fig. 8 Boundary-layer velocity distributions, P8 inlet model centerbody.

flowfield at the throat station, X = 49.5 in. The pitot pressure data represented by the circular symbols on Fig. 5 were obtained with the traversing probe at lateral station $Z = -2.095$ in. (Z is positive to the right of the model, looking upstream), whereas the triangular symbols delineate centerline results obtained with fixed rakes during another tunnel entry. The difference in level exhibited by the two sets of data for X = 49.5 in. between about Y' = 0.3 and 0.6 in. may be attributed to the effects of variations in model and wind-tunnel conditions and also to observed lateral variations in flow properties at the throat station. The pitot-pressure and total-temperature distributions shown in Figs. 5 and 6 indicate approximately the same boundary-layer thickness on the centerbody at X = 42.0 in. The total temperature distributions delineate a thinner viscous region on the cowl surface in comparison to the apparent boundary-layer edge indicated by the peaks in the pitot-pressure profiles. The original analytical predictions (solid lines) are compared to experimental data in Fig. 5. The predictions are terminated at the experimental boundary-layer thickness for each surface. The experimentally measured pitot pressures are lower than the prediction over nearly the entire passage height and the experimental shock wave is closer to the cowl surface at the station upstream of the interaction region (X = 42.0 in.). Farther downstream, at X = 49.5 in., the presence of the expansion and reflected shock wave modifies the experimental distribution to such an extent that the original prediction does not resemble the measured profile. Considerably better agreement was realized using the modified analytical procedures (dashed line in Fig. 5, X = 49.5 in.).

Composite experimental pitot-pressure distributions are shown superimposed upon the internal passage contours in Fig. 7. The paths of the cowl shock wave and its subsequent reflections are delineated by the discontinuities on the profiles. The pitot pressures near the cowl surface do not increase continuously with distance from the surface. This is a result of the compression between the cowl shock wave and the cowl surface. Poor overlapping of profile segments, attributed to a mismatch of tunnel conditions between tunnel runs, occurred at X = 47.0 in.

Boundary Layer

Two criteria were used in the determination of the boundary-layer thickness for purposes of data reduction:

1) The boundary-layer thickness was set equal to the height at the peak or immediately outside of the hump (when a hump was present) of the total-temperature distribution for all cowl stations and all centerbody stations except those with well-defined shock waves within the boundary layer.

2) For those cases with a well-defined shock wave within the boundary layer as determined by criterion (1), the boundary-layer thickness was equated to the height of the mid-point of the pitot-pressure change across the shock wave. Criterion (2) was applied at centerbody stations X = 45.5 and 46.0 in.

Several nondimensional centerbody velocity profiles are shown in Fig. 8. Little variation in profile shape was noted upstream of the interaction region, and the profile at X = 42.0 in. is typical. As shown in Fig. 7, the impinging shock wave enters the boundary layer at about X = 43.0 in. and the reflected shock wave emerges from the boundary layer at about X = 46.0 in. The centerbody boundary-layer downstream of X = 47.0 in. is free of strong disturbances. The continuous changes in the shape of the nondimensional velocity profiles through the centerbody interaction region between X = 42.0 and 45.0 in. are illustrated in Fig. 8. The shape of the profile at X = 46.0 in. is influenced by the shock wave at the edge of the boundary layer. Down-

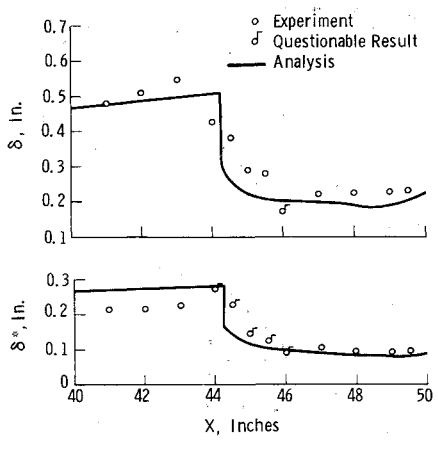

Fig. 9 Boundary-layer properties, P8 inlet model centerbody.

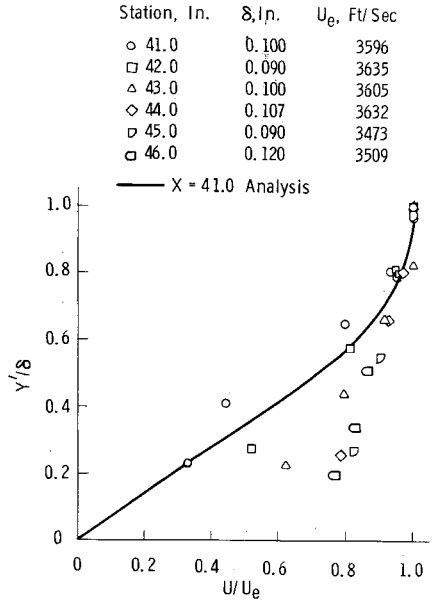

Fig. 10 Boundary-layer velocity distributions, P8 inlet model cowl.

stream of X = 46.0 in., the profile begins to recover the typical turbulent shape. The changes in profile shape downstream of X = 47.0 in. were small.[8]

The boundary-layer properties computed from the centerbody profile data are shown in Fig. 9. The boundary-layer thickness at X = 46.0 in. is flagged to indicate that the relatively low value results from the presence of a shock wave within the profile. The displacement thicknesses for X = 44.0 to 46.0 in. (flagged symbols) are questionable since the impinging and reflected shock waves are within the boundary layer at these stations, causing normal gradients in static pressure that were not accounted for in the calculations. The boundary-layer thickness parameters increase upstream of the interaction region (X = 41.0 through 43.0 in.) and then decrease rapidly across the interaction region (X = 46.5 in.). The redevelopment of the turbulent boundary layer downstream of the interaction region is characterized by a slight increase in thickness and a slight decrease in displacement thickness. The agreement between analysis and experiment is good for the thickness upstream of the interaction region and the displacement thickness downstream of the interaction region. The fair agreement for the displacement thickness in the upstream region and the thickness in the downstream region implies a corresponding fair agreement in profile shapes over the entire range. The observation that this is the case was reported in Ref. 8.

Several nondimensional cowl boundary-layer velocity profiles are shown in Fig. 10. The initial profile shape at X = 41.0 in. is similar to the analytical laminar profile shown for comparison. The shape of the profile changes rapidly between X = 41.0 and 43.0 in. and the boundary layer appears to be turbulent at X = 44.0 in. It was also determined from surface pitot-pressure distributions that transition occurred between X = 41.0 and 44.0 in. The profile shape does not change appreciably downstream of X = 44.0 in.

The streamwise variations in cowl boundary-layer thickness parameters are given in Fig. 11. The computed displacement thicknesses at X = 48.5 and 49.0 in. (flagged symbols) are results for regions of high normal pressure gradient and are questionable since the surface static pressure was used in the data reduction procedure. The experimental boundary-layer thickness is nearly constant from X = 41.0 to 45.0 in. Transition from laminar to turbulent boundary-layer flow is occurring in this region in an adverse pressure gradient (Fig. 4). A rapid increase in thickness is observed between X = 45.0 and 48.0 in. as the turbulent boundary layer develops in a region of nearly constant surface pressure followed by a region of favorable pressure gradient. The displacement thickness decreases in the region of high adverse pressure gradient upstream of X = 45.0 in., and then increases in the region of more rapid growth of the turbulent boundary layer between X = 45.0 and 48.0 in. Both thickness parameters

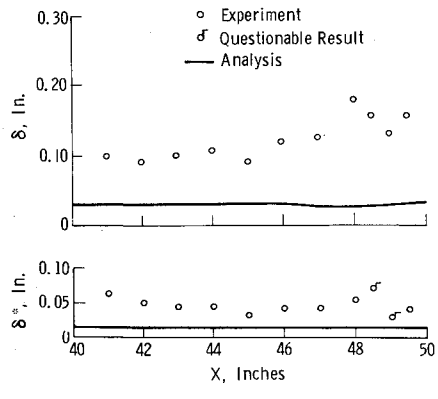

Fig. 11 Boundary-layer properties, P8 inlet model cowl.

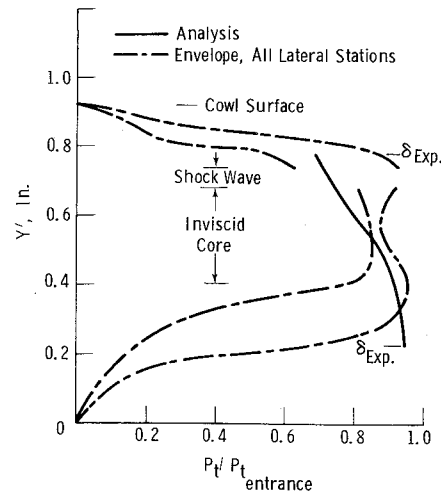

Fig. 12 Internal passage performance, P8 inlet model.

decrease across the region of shock-wave boundary-layer interaction. The analysis, which assumed that the boundary layer was laminar over the entire cowl surface, did not predict the observed boundary-layer growth. Revision of the analysis to account for the observed location of boundary-layer transition did not result in a significant improvement in the agreement between analysis and experiment.

Inlet Performance

Profiles of pitot pressure and static pressure were obtained at five lateral throat stations for the *P*8 inlet model. Distributions of Mach number and total pressure recovery were computed from the measured data. The experimentally determined Mach numbers at the throat station centerline were within the design range of 4.0–4.2 outside of the boundary layers. Larger variations in Mach number were observed near the sidewalls of the passage.

The lateral variations in total pressure recovery were small outside of the boundary layers; however, large variations were observed near the centerbody surface. The range of the measured recoveries for the inviscid core flow, based upon the tunnel freestream total pressure, was from about 0.60 to 0.77. With a representative inlet-entrance recovery of 0.8, the internal-passage recovery levels shown in Fig. 12 were obtained. The open band between Y' = 0.68 and 0.74 in. indicates a region in which the static pressure readings were affected by the presence of a shock wave in the vicinity of the tips of the probes. A representative recovery level for the core flow of the *P*8 internal passage is about 0.85 with an experimental variation of approximately ±0.10. In selecting this representative level, the extremely low recovery results between Y' = 0.2 and 0.4 in. (Fig. 12) were not considered. Only six data points were obtained within this region whereas many data points indicating higher recovery levels were obtained. The uncertainty of ±0.10 in recovery represents an uncertainty in range of approximately ±2.5% for the hypersonic cruise vehicle considered in this study.[1]

Additional recovery data are shown in Refs. 7 and 8 for the *P*2 and *P*12 inlet models. With the exception of variations in the shape of the distributions, the recovery profiles of Fig. 12 are representative of all inlets.

Conclusions

The experimental results and the comparisons with the analytical predictions presented in this paper and in Refs. 7 and 8 show that:

1) A high level of total pressure recovery of the internal passage, approximately 0.85 for the core flow, was achieved for each inlet design. Within the accuracy of the measurements, estimated at ±0.10, the recovery was in agreement with the predicted level and was independent of the internal compression ratio over the range from 2 to 12. This uncertainty in recovery represents an uncertainty in range of approximately ±2.5%.

2) The agreement between the original design predictions and experiment for the details of the internal flow was only fair. Although considerable improvement in this agreement was effected by modifying the analytical procedures, further improvement is required in the methods for predicting the details of the boundary-layer development through and downstream of regions of boundary-layer transition, the boundary-layer and inviscid flow development downstream of leading edges of small bluntness, and the detailed characteristics of shock-wave boundary-layer interactions including the flowfields downstream of interaction regions.

3) The analytical techniques based on inviscid flow calculations with corrections for the boundary-layer displacement thickness were sufficient to design high performance inlets, independent of the ability to accurately predict the details of the internal flowfields.

References

[1] Sanator, R. J., DeCarlo, J. P., Boccio, J. L., and Shannon, J. A., "Development and Evaluation of an Inlet for Scramjet-Powered Hypersonic Cruise Vehicles," TR-68-48, Vols. I, II, and III, April 1968, Air Force Flight Dynamics Lab., Wright Patterson Air Force Base, Ohio.

[2] Sanator, R. J., Boccio, J. L., and Shamshins, D., "Effect of Bluntness on Hypersonic Two-Dimensional Inlet Type Flows," CR-1145, Oct. 1968, NASA.

[3] Torrillo, D. T., and Savage, S. B., "A Brief Review of Compressible Laminar and Turbulent Boundary-Layer Separation," Rept. 2324, April 1964, Republic Aviation Corp., Farmingdale, N.Y.

[4] Clutter, D., and Smith, A. M. O., "Solution of the General Boundary Layer Equations for Compressible Laminar Flow, Including Transverse Curvature," Rept. LB 31009, Feb. 1963, Douglas Aircraft Corp., Long Beach, Calif.

[5] Seebaugh, W. R., and Childs, M. E., "Influence of Suction on Shock Wave-Turbulent Boundary Layer Interactions for Two-Dimensional and Axially Symmetric Flows," CR-1639, Sept. 1970, NASA.

[6] Pinckney, S. Z., "Semiempirical Method for Predicting Effects of Incident-Reflecting Shocks on the Turbulent Boundary Layer," TND-3029, Oct. 1965, NASA.

[7] DeCarlo, J. P., Shamshins, D., Seebaugh, W. R., and Doran, R., "Investigation of Hypersonic Flows in Large-Scale Model Internal Passages," Final Rept., Contract NAS2-5052, Rept. FHR 3824, Nov. 1969, Fairchild Hiller, Farmingdale, N.Y.

[8] Seebaugh, W. R., Doran, R. W., and DeCarlo, J. P., "Detailed Investigation of Flowfields within Large-Scale Hypersonic Inlet Models," Final Rept., Contract NAS2-5719, Rept. FHR 4000 (NASA CR-114305), April 1971, Fairchild Hiller, Farmingdale, N.Y.

[9] Rose, W. C., "A Method for Analyzing the Interaction of an Oblique Shock Wave with a Boundary Layer," TN D-6083, Nov. 1970, NASA.